

Density structures in perturbed thin cold discs

Miodrag Sremčević,¹* Frank Spahn¹ and Wolfgang J. Duschl²

¹*Institute of Physics, University of Potsdam, Am Neuen Palais 10, 14469 Potsdam, Germany*

²*Institute of Theoretical Astrophysics, University of Heidelberg, Tiergartenstr. 15, 69121 Heidelberg, Germany*

Accepted 2002 August 21. Received 2002 August 21; in original form 2002 June 12

ABSTRACT

We investigate the action of gravitational perturbers in thin cold astrophysical discs. The model includes viscous diffusion of the disc matter and gravitational scattering by the perturber as two counteracting processes. Two types of density structures are found, depending on the mass of the perturbing body and on the amount of momentum transport in the disc. A gap around the whole circumference of the disc is opened if the perturber is more massive than a certain threshold. Alternatively, a local S-shaped density modulation is generated that we call a ‘propeller’. We derive an analytic solution of the S-shaped density patterns using Green functions of the stationary problem. We find that the large-scale appearance of propellers does not depend on the details of the scattering process but mainly on the effective strength of the gravity perturbations – namely the amplitudes of the Green functions. The crucial disc parameter is the kinematic viscosity describing the transport properties of the disc material. The solution provides the characteristic spatial extensions of the structures depending on the mass of the perturber and the viscosity of the disc. Furthermore, we propose a new criterion for the threshold mass of the perturber needed to open a gap. The results are applied to dense planetary rings perturbed by an embedded moonlet, and to gas–dust discs around a protostar perturbed by a protoplanet. Concerning the rings of Saturn there is the chance to verify our findings with the high-resolution experiments of the Cassini spacecraft, which arrives at Saturn in 2004.

Key words: accretion, accretion discs – diffusion – hydrodynamics – scattering – planets: rings.

1 INTRODUCTION

Discs are common structures in the Universe found over a large range of spatial scales, such as for instance galaxies, active galactic nuclei, accretion discs around one component of a binary, protoplanetary gas–dust discs, our Solar system and planetary rings around the giant planets in our Solar system. The flattening of a disc is a result of angular momentum conservation during their formation and evolution. In this work, we concentrate on thin cold discs, i.e. objects such as planetary rings or protoplanetary accretion discs, where turbulent heating is negligible – all processes take place far away from the central body or the central body is not a massive object. The common property of these discs is that thermal (energetic) processes are of minor importance so that the balances of mass and momentum are sufficient to describe the dynamics of the system in the first approximation. Although planetary rings and protoplanetary discs are, in fact, very different in many respects, we will show that the dynamics of both cosmic objects can be described within the same

hydrodynamical approach, using a scaling for the geometry and the transport properties. Then, this treatment will be applied in order to explain certain types of structures (irregular fluctuations) observed in planetary rings, and alternatively, to describe density features in a preplanetary disc that might be caused by an embedded growing core of a planet.

Over the previous two decades a wealth of new structures has been found in planetary rings, mainly by the two Voyager missions (Smith et al. 1981, 1982; Esposito et al. 1983), but also through the steadily improving resolution of ground-based observational techniques (Poulet et al. 2000; Nicholson et al. 2000). A poorly understood type of structure in the main rings of Saturn, observed by the space probes, are the so-called irregular structures (Cuzzi et al. 1984; Horn & Cuzzi 1996) in rings with high optical depth $\tau > 1$. These density fluctuations have been seen down to the limit of the resolution of the experiments (≈ 100 m). One possibility to explain at least part of these irregular structures is an oscillatory instability driven by viscous transports in this granular disc (Schmit & Tscharnuter 1999; Schmidt et al. 2001 and references therein).

Alternatively, Hénon (1981) and Lissauer, Shu & Cuzzi (1981) suggested that larger bodies in planetary rings, from house-size up

*E-mail: msremac@agnld.uni-potsdam.de

to kilometres in size, could cause characteristic density features in the rings, recording in this way the upper part of the size distribution of the ring particles. The famous and the only example up to now has been the prediction of the existence of a moonlet in the Encke-division of the A ring of Saturn. Initial theoretical studies (Cuzzi & Scargle 1985; Showalter et al. 1986; Spahn & Sponholz 1989) indicated the presence of a moonlet, and later on a careful inspection of the Voyager imaging data by Showalter (1991) identified the satellite Pan. It is likely that the size distribution of ring particles includes a number of large objects that were still too small to be resolved by the Voyager cameras. A proof of their existence and a determination of their distribution provides a strong constraint on the origin of the ring – e.g. a catastrophic disruption of a parent satellite. Therefore, we will follow investigations concerning the action of embedded moonlets in planetary rings (Showalter et al. 1986; Spahn & Wiebcke 1988; Spahn & Sremčević 2000). The major goal of this paper is to derive analytical expressions for the spatial scalings and the extensions of the resulting structures. These findings provide useful tools for high-resolution observations, expected to come with the Cassini mission in 2004.

The other type of cosmic discs we are interested in here and that can be described within the theoretical framework of this paper, are protoplanetary discs with forming planets embedded. Since the pioneering observations by Mayor & Queloz (1995), extrasolar planets, i.e. planets orbiting stars other than the Sun, are no longer only a theoretical concept but proven facts. Given the current rate of detections, it seems that soon more than 100 planetary systems will be known. The fact that all observed planetary systems differ from the Solar system in that the planets are typically very massive and close to the central stars, in all likelihood is an observational selection effect caused by the search method applied (radial velocity modulations). It is less clear, however, whether the large eccentricities often found in the orbits of the planets may also be attributed to selection effects. Although all of these observations do not exclude planetary systems very similar to our planetary system, they demonstrate that the structure of the Solar system is not the only possible one for a planetary system. This observation alone already mandates a much closer inspection of the circumstances of planet formation.

Planets form in what is left of the protostellar accretion disc at a point in time when most of the initial mass of the disc is already accreted into the newly formed star. Then, the disc is relatively cold, the self-gravity of the disc is of minor importance and the disc may be envisaged as a mixture of gas, dust and planetesimals. As soon as one planetesimal has grown sufficiently in mass, for instance as a result of a runaway growth process, it will act as a perturbing body in the protoplanetary accretion disc, similar to the case of a moonlet in a planetary ring. The formation and evolution of a protoplanet and its orbit are closely related to the interaction between the disc and the protoplanet. Thus, the understanding of this interaction is important for the explanation of the appearance and the properties of planetary systems.

The action of a Jupiter-sized planet embedded in a solar nebula has been investigated numerically in detail by Kley (1999) and other authors (for instance, Lubow, Seibert & Artymowicz 1999; Bryden et al. 2000; Artymowicz 2000; Kley, D’Angelo & Henning 2001) in the hydrodynamic limit. They found that a gap is opened around the orbit of the planet. The planet exerts gravitational torques on the neighbouring disc material thereby depleting the disc density. Counteracting this process is a viscous diffusion that tends to refill the depleted region. From the balance of these torques it was estimated (Lin & Papaloizou 1986) that approximately a Neptune-sized planet is the threshold for opening up a gap for parameters

typical of protoplanetary discs. Simulations carried out recently by Artymowicz (2000) yield a smaller limiting mass.

Here we focus on the situation of embedded protoplanets below or close to this mass threshold. Then we can expect a local density modulation to be created instead of the formation of a complete gap. Using the standard Shakura & Sunyaev (1973) viscosity prescription, we apply our analytical solution to this case as well. We also propose a new criterion for estimating the mass threshold for opening of a gap. While direct observations of protoplanetary circumstellar discs with sufficient spatial resolutions are not possible today, in the future telescopes such as ALMA, for instance, might allow a direct verification of these model predictions.

The paper is organized as follows. In Section 2 we present the hydrodynamic model with a probabilistic description of the gravitational scattering of the perturber. The method of calculating the complex scattering process is given in Section 2.3. In the remainder of Section 2 a direct numerical solution of the model is presented for comparison. In Section 3 an analytic solution is constructed that is based on a Green function formalism and is used to evaluate the spatial extensions of the induced density structures. Applications are discussed in Section 4, where Section 4.1 is devoted to the discussion of the scalings and spatial extensions of stationary density structures. Then, we separately discuss applications to protoplanetary discs and planetary rings. The main results are summarized in Section 5.

2 THE MODEL: HYDRODYNAMICAL FLOW AND PROBABILISTIC SCATTERING

The region of gravitational influence of a body embedded in a disc is given by its Hill radius

$$h = a_0 \left[\frac{M_p/M_c}{3(1 + M_p/M_c)} \right]^{1/3},$$

where a_0 is the semimajor axis of the perturber, M_p is its mass and M_c is the mass of the central body. The corresponding dimensionless scale is denoted by $h^* = h/a_0$. This extent $O(h)$ of the region of gravitational influence is rather small compared with the whole circumference of the disc. For instance, the Hill radius of the moon of Saturn Pan is approximately $h \approx 10^{-4}a_0$ and for Earth–Sun system it is $h \approx 0.01a_0$. Thus, we may separate the model disc into two different regions (Spahn & Wiebcke 1988), namely the scattering region and the rest of the disc. Furthermore, we assume that the scattering region can be approximated by a line connecting the central body and the perturber. The dynamics characterizing the scattering region is modelled with a probabilistic concept. The disc apart from the scattering line is described by hydrodynamic equations. In the following we assume that the perturber moves in a Keplerian circular orbit.

2.1 Hydrodynamic description

The equations of motion are given by the balance laws for mass and momentum. We use the thin-disc approximation with the vertically averaged balance equations

$$\partial_t \Sigma + \nabla \cdot (\Sigma \mathbf{u}) = 0, \quad (1)$$

$$\Sigma \partial_t \mathbf{u} + \Sigma (\mathbf{u} \cdot \nabla) \mathbf{u} = \Sigma \mathbf{f} - \nabla \cdot \mathbf{P}. \quad (2)$$

Here Σ , \mathbf{u} , \mathbf{f} and \mathbf{P} are the surface density, the mean velocity, external forces and the pressure tensor, respectively. The latter is given in Newtonian form as

$$\mathbf{P} = p \mathbf{I} - 2\Sigma\nu \mathbf{D} - \Sigma\zeta(\nabla \cdot \mathbf{u}) \mathbf{I},$$

where \mathbf{I} is the unit tensor. The vertically averaged pressure, the kinematic bulk and shear viscosity are denoted by p , ζ and ν , respectively. \mathbf{D} is the traceless shear tensor

$$\mathbf{D} = \frac{1}{2} (\{\nabla, \mathbf{u}\} + \{\nabla, \mathbf{u}\}^T) - \frac{1}{3} (\nabla \cdot \mathbf{u}) \mathbf{I},$$

where $\{\mathbf{x}, \mathbf{y}\}$ denotes the dyadic product of two vectors. With these constitutive equations the balance laws are the continuity and the Navier–Stokes equation. The mean velocity is dominantly Keplerian

$$\mathbf{u} = u_r \mathbf{e}_r + r\Omega \mathbf{e}_\varphi, \quad \Omega(r) = \sqrt{GM_c/r^3},$$

where cylindrical coordinates are used. The radial component of the velocity u_r is much smaller than the Keplerian velocity $|u_r| \ll r\Omega$, and a small azimuthal non-Keplerian component is neglected. Focusing on stationary structures ($\partial_t \mathbf{u} = 0$) and neglecting self-gravity we obtain from the azimuthal component of the momentum balance (2) the following relation (Lynden-Bell & Pringle 1974; Pringle 1981; Stewart, Lin & Bodenheimer 1984)

$$r \Sigma u_r = -3\sqrt{r} \partial_r (\sqrt{r} \nu \Sigma). \quad (3)$$

Its derivation requires the assumption of either axisymmetry or that terms of the form $r^{-1} \partial_\varphi u_r$ are negligible with respect to $\partial_r u_r$. Inserting equation (3) into the continuity equation (1) (written in cylindrical coordinates), and using a frame corotating with the perturber we obtain

$$\partial_t \Sigma + [\Omega(r) - \Omega_0] \partial_\varphi \Sigma - \frac{3}{r} \partial_r [\sqrt{r} \partial_r (\sqrt{r} \nu \Sigma)] = 0. \quad (4)$$

The equation describes the viscous diffusion of the material in the disc. Although we consider stationary structures, the first term $\partial_t \Sigma$ is kept in the numerical simulations. The remaining equation (4) describes a stationary pattern created by the two counteracting processes: gravitational scattering as a permanent source of perturbations and viscous diffusion of the material as a relaxing reaction. It obeys the typical form of a diffusion equation with $[\Omega(r) - \Omega_0] \partial_\varphi$ instead of the time derivative ∂_t .

The crucial disc parameter is the kinematic viscosity ν . In order to cover similar properties of different types of cosmic discs we have to choose a reasonable model for this parameter. In general, ν may be a function of local conditions in the disc, that is, a function of the surface density Σ and the disc temperature (velocity dispersion c). Some additional flexibility of the model can be achieved if one assumes that the kinematic viscosity may also depend on the radial distance, time and the thickness of the disc. For the purpose of this work we use the power-law dependence of the kinematic viscosity on the surface density and the radial distance (Lin & Pringle 1987; Wisdom & Tremaine 1988; Schmit & Tscharnuter 1999):

$$\nu = \nu_0 \left(\frac{\Sigma}{\Sigma_0} \right)^\beta \left(\frac{r}{a_0} \right)^\gamma. \quad (5)$$

The formula does not include a dependence on the velocity dispersion, since the model is isothermal. For the unperturbed disc with the surface density Σ_0 the expression (5) gives a nominal value ν_0 for the viscosity at the position of the perturber a_0 . Here, the radial dependence is not of importance, since the region of interest is very narrow (of the order of the Hill scale h). We display it in equation (5) in order to allow for a comparison with analytic solutions of similar problems (Lynden-Bell & Pringle 1974; Pringle 1981; Lin & Pringle 1987).

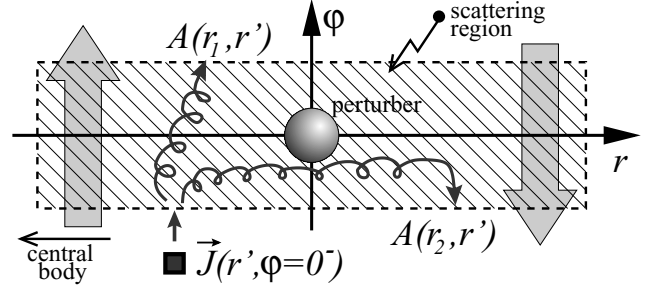


Figure 1. The probabilistic approach to the scattering process. An element of the disc material, with mass flux J , is approaching the perturber, and as a result it can be scattered almost anywhere. We assign the probability $A(r, r')$ for a scattering from the initial position r' to a final one at r . The big grey arrows represent the Keplerian shear $(\Omega - \Omega_0)r$.

2.2 Probabilistic modelling of the scattering process

The rather complicated gravitational scattering of the perturber is modelled by a probabilistic Markov-chain model (Spahn & Wiebicke 1988). This approach is motivated by chaotic behaviour of single-particle trajectories in the vicinity of the perturbing body (Petit & Hénon 1986). Instead of following the very complicated and computationally demanding motion of the fluid in the proximity of the perturber, we consider probabilistic transitions between radial positions.

In the corotating frame material enters the scattering line from positions $(r' < a_0, \varphi = 0^-)$ and $(r' > a_0, \varphi = 0^+)$, where it is scattered by the gravitational attraction of the perturber to $(r < a_0, \varphi = 0^+)$ or $(r > a_0, \varphi = 0^-)$ (see Fig. 1). The Markov-chain model of that process is

$$|J_\varphi(r, \varphi = 0^\pm)| = \int dr' A(r, r') |J_\varphi(r', \varphi = 0^\mp)|, \quad (6)$$

where $A(r, r') dr dr'$ is the probability that matter is scattered from $(r', r' + dr')$ to $(r, r + dr)$. In the following primed quantities refer to the situation prior to scattering and unprimed ones to the situation after. The \pm signs in the superscripts in equation (6) are chosen according to the sign of the relative angular velocity $\Omega(r) - \Omega_0$. The azimuthal component of the mass flux vector of the disc material in the corotating frame is given by

$$J_\varphi(r, \varphi) = \Sigma(r, \varphi) r [\Omega(r) - \Omega_0]. \quad (7)$$

The integration of the mass balance equation (1) over the volume of the considered scattering region gives a condition for the kernel $A(r, r')$,

$$\int A(r, r') dr = 1, \quad (8)$$

expressing the conservation of mass.

The dynamics of our model disc with an embedded perturber is closed with equations (4)–(7), provided the scattering matrix $A(r, r')$ is calculated. Then, the self-consistent solution of equations (4) and (6) gives the stationary surface density field $\Sigma(r, \varphi)$.

2.3 Scattering matrix

In order to determine a scattering matrix $A(r, r')$ we numerically integrate the equations of the restricted three-body problem (RTB) for a set of test particles, where the perturber is assumed to be a point mass. From the initial and final orbital elements of these test particles, taken before and after their encounter with the perturber,

we calculate the scattering matrix $A(r, r')$ by orbit averaging. The velocity dispersion of the disc is taken into the account through parameters of the distribution of initial eccentricities and inclinations. In the following, we first display the method and then we present the numerical results.

The dynamics of test particles in a corotating frame is given by

$$\ddot{\mathbf{r}} + 2\boldsymbol{\Omega}_0 \times \dot{\mathbf{r}} + \boldsymbol{\Omega}_0 \times (\boldsymbol{\Omega}_0 \times \mathbf{r}) = -\nabla\Phi_c - \nabla\Phi_p, \quad (9)$$

where Φ_c and Φ_p are the potential of the central body and the perturber, respectively. The spatial vector of a particle is denoted by \mathbf{r} and the dots denote the time derivative. For a very small secondary body, equation (9) can be linearized to give Hill's equations in a dimensionless form

$$\ddot{\tilde{x}} = 2\dot{\tilde{y}} + 3\tilde{x} - 3\tilde{x}/s^3 + O(h^*), \quad (10)$$

$$\ddot{\tilde{y}} = -2\dot{\tilde{x}} - 3\tilde{y}/s^3 + O(h^*), \quad (11)$$

$$\ddot{\tilde{z}} = -\tilde{z} - 3\tilde{z}/s^3 + O(h^*), \quad (12)$$

where $\tilde{x} = (x - a_0)/h$, $\tilde{y} = y/h$ and $\tilde{z} = z/h$ are scaled Cartesian coordinates measured from the perturber. The time derivative is denoted by $\dot{\tilde{x}} = \partial\tilde{x}/\partial(\Omega_0 t)$ and $s^2 = \tilde{x}^2 + \tilde{y}^2 + \tilde{z}^2$ is the distance from the perturber. Equations (10)–(12) are nearly independent of the mass of the secondary body. Thus, the problem is naturally described in the following scaled variables (Petit & Hénon 1986; Ida & Makino 1992):

$$b = \frac{r - a_0}{h}, \quad \tilde{a} = \frac{a - a_0}{h}, \quad \tilde{e} = \frac{e}{h^*}, \quad \tilde{i} = \frac{i}{h^*}, \quad (13)$$

where b , \tilde{a} , \tilde{e} and \tilde{i} are the scaled radial coordinate, semimajor axis, eccentricity and inclination, respectively.

The first step in the procedure is to choose a proper phase-space distribution function of initial coordinates for the set of test particles. Various authors have studied this problem (Petit & Hénon 1987; Ida & Makino 1992; Lissauer 1993; Ohtsuki & Emori 2000) and they found that eccentricities \tilde{e} and inclinations \tilde{i} obey Rayleigh distributions

$$f(\tilde{e}, \tilde{i}) = \frac{2\tilde{e}}{\tilde{e}_0^2} \exp\left(-\frac{\tilde{e}^2}{\tilde{e}_0^2}\right) \frac{2\tilde{i}}{\tilde{i}_0^2} \exp\left(-\frac{\tilde{i}^2}{\tilde{i}_0^2}\right). \quad (14)$$

It is normalized to unity, and parameters \tilde{e}_0 and \tilde{i}_0 are the root mean square (rms) values: $\tilde{e}_0^2 = \langle \tilde{e}^2 \rangle$ and $\tilde{i}_0^2 = \langle \tilde{i}^2 \rangle$. The other orbital elements are assumed to be uniformly distributed. The distribution of random velocities, related to equation (14), is a triaxial Gaussian distribution in cylindrical coordinates (Lissauer 1993):

$$f(z, \mathbf{v}) = \frac{\Omega}{2\pi^2 c_r^2 c_z^2} \exp\left(-\frac{v_r^2 + 4v_\phi^2}{2c_r^2} - \frac{v_z^2 + \Omega^2 z^2}{2c_z^2}\right),$$

where

$$2c_r^2 = \tilde{e}_0^2 r^2 \Omega^2, \quad 2c_z^2 = \tilde{i}_0^2 r^2 \Omega^2.$$

The ratio of the rms inclination to the rms eccentricity is found to vary from 0.5 to 1 in different problems (Ida & Makino 1992; Lissauer 1993; Ohtsuki & Emori 2000). Since we find that the contribution caused by the distribution of inclinations does not play a significant role in our model, we fix this value to be 1. Then a single velocity dispersion c_0 characterizes the unperturbed disc and the corresponding rms eccentricities and inclinations are given by

$$\tilde{e}_0 = \tilde{i}_0 = \frac{1}{\sqrt{2}} \frac{c_0}{a_0 \Omega_0}.$$

Here, the Kepler velocity $r\Omega$ is taken at the position of the perturber, since the region of interest is narrow. Thus, the scattering matrix is

characterized by the single parameter: the effective velocity dispersion c_0 (or equivalently $\tilde{e}_0 = \tilde{i}_0$).

The calculation of the kernel $A(r, r')$ proceeds as follows. First, the trajectories of a set of test particles with the distribution function (14) of the orbital elements are obtained by solving the equations (9) numerically. For each run the initial and the final elements are recorded. Then we discretize the model disc into concentric cylindrical shells, labelled by the index j , in intervals (r_j, r_{j+1}) . The cylinders $r = r_j$, i.e. the borders of the shells, are normal to the plane of the motion of the perturber. The matrix $A(j, j')$ is then given by (Spahn & Wiebicke 1988)

$$A(j, j') = \Delta N(j, j')/N(j'),$$

where $N(j')$ is the number of particles initially in shell j' and $\Delta N(j, j')$ is the fraction of particles ending in shell j . These numbers are calculated using the relations

$$N(j') = \sum_n p_1^{(n)}(j'), \quad \Delta N(j, j') = \sum_n p_1^{(n)}(j') p_F^{(n)}(j),$$

where the summation is over all test particles. The probability that the initial (final) orbit of the particle n is found in the radial annulus j is denoted by $p_{1/F}^{(n)}(j)$. We relate the probability p to the orbital elements averaging over the trajectory of the particle: $p = \Delta t/T$, where Δt is the time the particle spends in the annulus j between (r_j, r_{j+1}) , and T is the orbital period. Then the probability p is calculated numerically using Kepler's equation and projecting the trajectories on to the plane of motion of the perturber.

For the numerical calculations we divide the model disc into 400 concentric equidistantly separated cylindrical annuli covering the interval $b \in [-20, 20]$. The test particles are started at an azimuthal distance of $1000h$ from the perturber, and the integration of the equations of motion is stopped at the same azimuthal separation distance. These limits ensure that the region of the interaction is well included in the integration. The numerical integration is carried out using a Runge–Kutta method of fifth order for parameter \tilde{e}_0 from 0.005 up to 0.5. We also simulated two-dimensional (2D) situations with $\tilde{i} = 0$ and found practically no difference with respect to the three-dimensional case in the resulting scattering matrix. This is a consequence of the fact that we consider small inclinations and the projected trajectory does not differ significantly from the 2D case.

The resulting scattering matrices $A(j, j')$ are shown in Fig. 2, corresponding to different values of \tilde{e}_0 . Depending on the initial impact parameter b_1 , three regions can be identified.

- (i) The region of horseshoe orbits $|b_1| < 2$ – test particles are deflected by the perturber, resulting in $b_F \approx -b_1$ and $e_F \approx e_1$.
- (ii) Non-regular trajectories (see, for instance, Petit & Hénon 1986) for $|b_1| \in (2, 4)$ – test particles are scattered everywhere beyond $b_F > 2$, thus clearing the space around the perturber (Fig. 3).
- (iii) Negligible changes of orbital elements for $|b_1| > 4$.

The point-mass assumption for the perturber has no consequence for our scattering concept. For instance, a moonlet in the B-ring of Saturn with parameters as given in Table 1, has a diameter of approximately 1.5 Hill scales. Particles originating from region (ii) will, in fact, collide with the moonlet, and thus, be removed from the disc. In the cases of the point-mass perturber the same particles will be scattered out of the region (ii) where they originate, which means that they are also removed. In the case of both model assumptions for the perturber these particles disappear in the statistical concept and do not change the resulting stationary structures. In the case of a planetary core in an accretion disc, the consideration of its finite size would correspond to accretion of material. In our model the

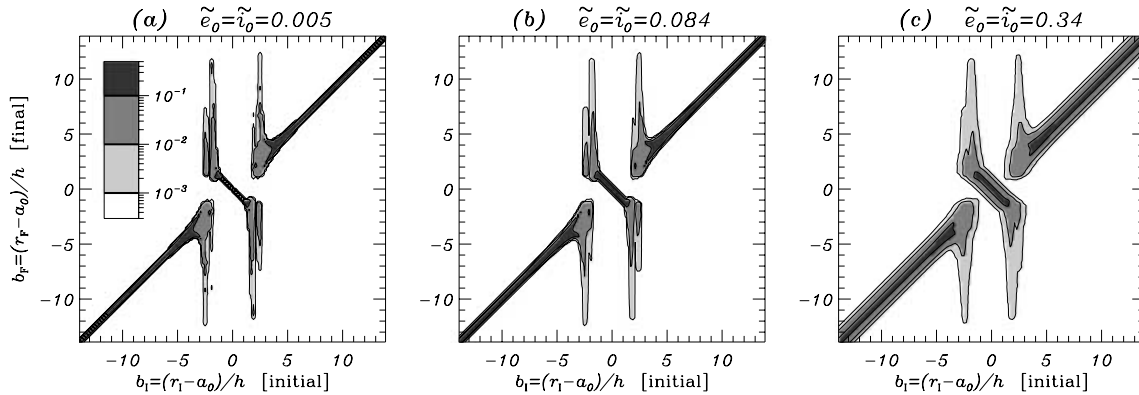


Figure 2. The scattering matrix $A(r_F, r_I)$ calculated from numerical integration of a set of test particles: (a) $\tilde{e}_0 = \tilde{i}_0 = 0.005$, (b) $\tilde{e}_0 = \tilde{i}_0 = 0.084$ and (c) $\tilde{e}_0 = \tilde{i}_0 = 0.34$. With decreasing h^* (or increasing eccentricity) features become broader: the effective velocity dispersion is increasing. Note that matrices are point-symmetric with respect to $(0, 0)$ – because of the symmetry of RTB equations.

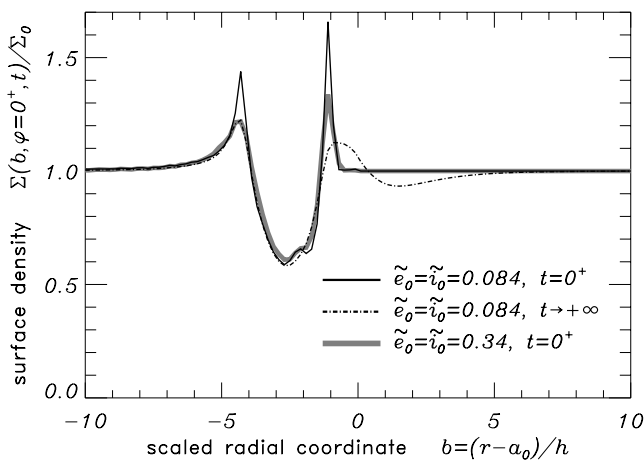


Figure 3. The radial profiles of the surface density in the close vicinity of the perturber. The different graphs represent the initial (solid lines) and final (stationary) density profiles (chain line). The thick grey line shows an initial profile where an increased effective velocity dispersion smears out the density contrasts.

point-mass assumption ensures conservation of the total mass in the disc according to equation (8).

The shape formed by the dominant elements of the matrix $A(r_F, r_I)$, Fig. 2, closely follows the shape of the final semimajor axis versus the initial one $a_F(a_I)$. The broadening of the line is caused by the initial distribution of eccentricities and inclinations. Neglecting the inclinations for the moment, the trajectory of a test particle is

Table 1. Adopted B ring of Saturn and moon parameters for numerical simulations.

	Parameter	Value
Ring	Surface density	$\Sigma_0 = 100 \text{ g cm}^{-2}$
	Optical depth	$\tau_0 = 1$
	Kinematic viscosity	$\nu_0 = 10 \text{ cm}^2 \text{ s}^{-1}$
	$\partial(\log \nu)/\partial(\log \Sigma)$	$\beta = 1.25$
	$\partial(\log \nu)/\partial(\log r)$	$\gamma = 0$
	Velocity dispersion	$c_0 = 0.2 \text{ cm s}^{-1}$
Moon	Semimajor axis	$a_0 = 10^5 \text{ km}$
	Orbital frequency	$\Omega_0 = 1.95 \times 10^{-4} \text{ s}^{-1}$
	Bulk density	$\rho = 1000 \text{ kg m}^{-3}$

$r = a + a e \cos(\varphi + \varphi_0)$. The radial width covered by the trajectory is simply $\delta b = 2\tilde{e}$, and the broadening of the matrix from the line $a_F(a_I)$ is approximately $2\tilde{e}_0$. This is clearly seen in Fig. 2, which shows $A(r_F, r_I)$ for different values of \tilde{e}_0 . For the cases of $\tilde{e}_0 < 0.1$ the resulting matrices differ only slightly from each other. Since the radial scale is equal to the Hill radius h , we can estimate that the limit of applicability of the scattering matrix model is approximately $\tilde{e}_0 < 0.5$.

2.4 Numerical simulations

In this section we present a numerical solution of equations (4)–(7) (see also Spahn & Sremčević 2000). First, we briefly describe the numerical method, and then we display the results.

The integral equation (6) is approximated by a discrete sum resulting in a matrix equation involving the discrete scattering matrix $A(j, j')$. The diffusion equation (4), including the time derivative of the surface density, is solved using a finite-difference method. Although we are seeking stationary structures, the time derivative term is kept in the numerical algorithm because the parabolic-type of partial differential equation (PDE) is suitable for relaxation methods with given boundary conditions. In order to test the numerical methods we have applied different mesh grids (uniform or adaptive), and difference methods (implicit or explicit), and different initial conditions and sizes for the simulated region. In all cases we have obtained the same stationary structure. Concerning the time efficiency of the numerical algorithm, the best results have been obtained with an explicit forward time centred space (FTCS) scheme with upwind differencing of the angle φ using a uniform mesh. Consequently, we adopt this method in our calculations. In this case, the stability criterion of the algorithm time, radial and angle step size is given by the corresponding Courant condition. For boundary conditions and the initial setup we use the unperturbed surface density Σ_0 .

In Fig. 3 we display radial profiles of the surface density in close vicinity to the perturber at $\varphi = 0^+$. This corresponds to a density profile along the horizontal line above the perturber in Fig. 1, at the upper border of the scattering region. The solid line displays the initial profile after the first time-step of the numerical algorithm ($t = 0^+$)

$$\begin{aligned} \Sigma(r < a_0, \varphi = 0^+, t = 0^+) \\ = \frac{\Sigma_0}{r|\Omega(r) - \Omega_0|} \int dr' A(r, r') r' |\Omega(r') - \Omega_0|, \end{aligned} \quad (15)$$

corresponding to a single scattering process for the disc matter. On the right-hand side of the perturber ($b > 0$ in Fig. 3) the material approaches from the unperturbed region so that $\Sigma \approx \Sigma_0$, and thus, the density is unchanged there. This profile already represents the essential features: particles are rearranged and a depletion is created around $b \approx -2.5$. Material is pushed partly toward the radial position of the perturber (right-hand peak in Fig. 3) and mostly to the opposite side (left-hand peak).

The final (stationary) profile (chain curve in Fig. 3) results from the combined long-term action of diffusion and gravitational scattering. For small perturber masses (shown in the plot) it is similar to the initial profile. The differences between them is found mainly in radial regions $b > 0$. The question is, how can a density perturbation show up at $b > 0$ in the case of low-mass perturbers where the structures cannot survive a synodic period? This is because a fraction of the disc matter recently scattered by the perturber and located close to its mean radial position, will later cross this radius driven by the diffusion. Thus, the motion with respect to the perturber is reversed and the density modulation again approaches the scattering region from the opposite direction. This happens in times much shorter than the synodic period. The results of these diffusion driven effects are more or less pronounced density modulation at $b > 0$ visible in Fig. 3. In contrast, in the case of massive perturbers the induced density variations at $b > 0$ will survive a synodic period and will also show up there [feature (i) below]. Moreover, if gravitational scattering dominates strongly (i.e. the diffusion is rather weak) the final profile becomes almost symmetric with respect to $b = 0$ (Spahn & Wiebcke 1988).

As a consequence of these processes, two types of resulting structures (Spahn & Sremčević 2000) evolve depending on the mass of the perturber:

- (i) a gap around the circumference of the disc (Fig. 4b);
- (ii) an S-shaped density modulation, or ‘propeller’, located around the perturber (Fig. 4a).

The first type of structure, i.e. a gap, evolves if the perturber is more massive than some threshold value ($h > h_{\text{crit}}$). Otherwise ($h < h_{\text{crit}}$) we obtain the propeller-shaped pattern centred at the location of the perturber. For perturber sizes between h_{crit} and several h_{crit} the density modulation extends over the whole circumference, but the region is not completely empty of material. For bigger perturbers the gap is fully developed.

By testing different models for the kinematic viscosity $\nu \propto \Sigma^\beta$, we find that there is no essential difference in the resulting structures. For $\beta > 0$ structures are azimuthally shorter, compared with the case with the constant viscosity ($\beta = 0$). The azimuthal profiles fall almost on top of each other provided that the scaling derived below is applied (Section 4.1, Fig. 9). The only difference is that the radial profiles become somewhat sharper for $\beta > 0$. It is worthwhile to note that this insensitivity with respect to the functional form of the transport coefficients is of decisive importance for the applications of the treatment presented here. It means that though the physics of the viscous transport in protoplanetary discs and in planetary rings are very different, their dynamics can still be described with the theory presented here.

3 ANALYTIC SOLUTION

The method described in this Section is to some extent similar to the solution of the time evolution of a viscous axisymmetric disc (equation 4 without the angle dependence) developed by Lüst (1952) and analysed by Lynden-Bell & Pringle (1974). Both solutions are

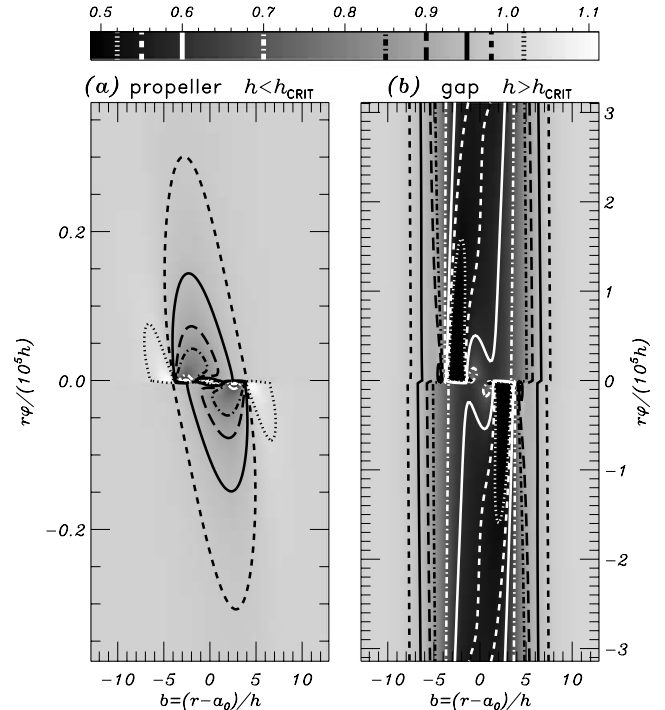


Figure 4. Grey-scale plot with isolines for two typical resulting density structures $\Sigma(r, \varphi)/\Sigma_0$: (a) ‘propeller’ for a case of the small perturber and (b) a gap for a perturber that is more massive than some threshold value. The density modulations are very elongated along the azimuthal axis compared with the radial extension ($> 10^3$), and in the case of the gap that covers the whole circumference of the disc. Structures are point-symmetric with respect to the location of the perturber $b = \varphi = 0$.

constructed using Green functions. The major difference is that Lüst considered the time evolution of an axisymmetric disc, and here we seek a stationary non-axisymmetric solution for a perturbed disc. Thus, we have to consider the results of the scattering process as a boundary condition at $\varphi = 0$, while Lüst assumed the Dirac pulse as an initial condition. Before going into detail, we briefly outline the method.

In this section we construct a solution for the hydrodynamical part of the model, assuming that the boundary condition is given by the final state of the Markov process. In turn, the hydrodynamic solution then determines the initial state for the Markov process. The two parts of the model determine the solution in a self-consistent way. Furthermore, in Section 3.1 we discuss the boundary conditions and a general solution of the expanded diffusion equation in the case of a constant coefficient for the viscosity. The general solution is given as an integral over one-mode solutions with unknown amplitudes. Since the one-mode solutions are non-orthogonal, it is difficult to calculate the amplitudes. In Section 3.2 we derive an approximation to the Green functions by calculating amplitudes of one-mode solutions for this special case. The solution of the model is an integral over Green functions, but in this way the amplitudes of Green functions are simply equal to the radial profile that serves as a boundary condition. Some effects of the power-law-dependent kinematic viscosity $\nu \propto \Sigma^\beta$ are discussed in Section 3.3.

3.1 General solution

In this section we consider the case of a constant kinematic viscosity ν_0 ($\beta = \gamma = 0$). In this way the diffusion equation (4) becomes linear

and we can employ the usual methods for solving it. This is not a serious restriction, since it turns out that the non-linearity does not change the character of the resulting structures very much. The perturbation σ of the surface density Σ gives

$$\Sigma(r, \varphi) = \Sigma_0 + \sigma(r, \varphi),$$

which is used in the following as the basic quantity.

First, we expand curvature terms ($\sim r^d$) and the Kepler velocity ($\sim r^{-1/2}$) around the position of the perturber ($b=0$) in powers of the Hill scale h^* , yielding the diffusion equation

$$Kb \partial_\varphi \sigma = -\partial_b^2 \sigma + O(h^*) \quad (16)$$

where K labels a dimensionless (in radians) constant depending on the parameters of the disc and the perturber:

$$K = \frac{\Omega_0 a_0^2}{2v_0} h^{*3}. \quad (17)$$

Besides the Hill radius h , equation (16) contains a second characteristic length-scale: $a_0 K$. Since the scattering matrix $A(b, b')$ is nearly independent of the disc properties we conclude that the stationary solution of the surface density field will only depend on scaled coordinates b and $\phi = \varphi/K$ (see equations 13). This means that the radial extent scales with h and the azimuthal extent scales with $a_0 K$.

The next step in the procedure is to choose proper boundary conditions. The basic equations (6), (10)–(12) and (16) are point-symmetric with respect to the position of the perturber ($b = \varphi = 0$), and thus, it is sufficient to consider one-half of the disc plane. Here we have chosen $\varphi > 0$ and the boundary conditions of the problem (Fig. 5a):

$$\sigma(b < 0, \varphi = 0^+) = g(b), \quad (18)$$

$$\sigma(b > 0, \varphi \rightarrow +\infty) = 0, \quad (19)$$

$$\sigma(b \rightarrow +\infty, \varphi) = 0, \quad (20)$$

$$\sigma(b \rightarrow -\infty, \varphi) = 0. \quad (21)$$

The first two relations together provide the boundary condition at the scattering line for the variable φ . It splits because the direction of the Keplerian flow reverses at $b=0$, which divides the disc into two parts. More importantly, the conditions (18) and (19) characterize the Markov process at the scattering line. The segment ($b > 0, \varphi = 0^+$) resembles the unperturbed state, whereas the part ($b < 0, \varphi = 0^+$) has already experienced the scattering process that is described by the function $g(b)$. In order to describe the latter, equation (15) has been chosen as a first approximation. Furthermore, equations (18) and (19) simply reflect the neglect of the periodicity of the Kepler disc, i.e. the density perturbations do not survive a path around the whole circumference of the disc. In other

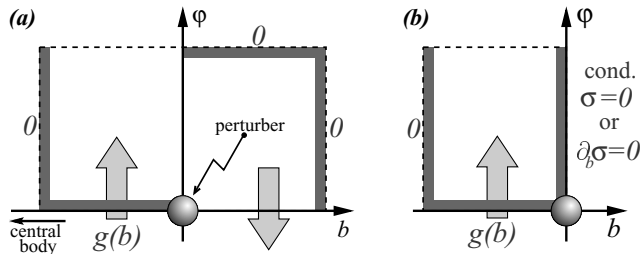


Figure 5. Boundary conditions for the analytic solution: (a) exact problem, equations (18)–(21); (b) approximate approach, equations (18) and (20), together with condition (i) or (ii) from Section 3.2.1. The arrows point to the direction of the Keplerian shear flow $(\Omega - \Omega_0)r$.

words, the conditions (18)–(21) are only suitable for propeller-type structures, i.e. in cases where the perturber is not massive enough to clear a gap. Finally, conditions (20) and (21) belong to the radial variable b and ensure that the perturbations vanish at $|b| \rightarrow \infty$.

Using the separation of variables and introducing the separation constant $-\lambda^2$, the single-mode solution of equation (16) reads

$$\sigma_\lambda(b, \varphi) = \exp\left(-\lambda^2 \frac{\varphi}{K}\right) (A_\lambda \text{Ai}[\lambda^{2/3} b] + B_\lambda \text{Bi}[\lambda^{2/3} b]), \quad (22)$$

where $\text{Ai}[z]$ and $\text{Bi}[z]$ are Airy functions (Abramowitz & Stegun 1970). They are two independent solutions of the differential equation $w''[z] = z w[z]$, which can be expressed as a combination of ordinary Bessel functions $J_n(\xi)$ and modified Bessel functions $I_n(\xi) = (-i)^n J_n(i\xi)$ of the order $n = \pm 1/3$:

$$\text{Ai}[z] = \begin{cases} \sqrt{-z} [J_{-1/3}(\xi) + J_{1/3}(\xi)]/3, & z < 0 \\ \sqrt{z} [I_{-1/3}(\xi) - I_{1/3}(\xi)]/3, & z > 0 \end{cases} \quad (23)$$

$$\text{Bi}[z] = \begin{cases} \sqrt{-z/3} [J_{-1/3}(\xi) - J_{1/3}(\xi)], & z < 0 \\ \sqrt{z/3} [I_{-1/3}(\xi) + I_{1/3}(\xi)], & z > 0, \end{cases} \quad (24)$$

where $\xi = 2|z|^{3/2}/3$. These functions are oscillatory for $z < 0$, while they are exponentially growing (Bi) or decaying (Ai) for $z > 0$. In order to satisfy the conditions (18)–(21) the coefficients B_λ must vanish. Then, the ‘scattering’ function $g(b)$ determines the coefficients A_λ . Thus, the general solution of equation (16) can be written as

$$\sigma(b, \varphi) = \int_0^\infty d\lambda A_\lambda \exp\left(-\lambda^2 \frac{\varphi}{K}\right) \text{Ai}[\lambda^{2/3} b]. \quad (25)$$

Unfortunately, in contrast to Bessel functions, the Airy functions do not form an orthogonal set of functions. Thus, different amplitudes A_λ will not decouple when trying to derive them from the source function $g(b)$. We shall overcome this in the next section, but here we display a discrete version of the solution (25):

$$\sigma(b, \varphi) = \sum_{n=0}^\infty A_n \exp\left(-\lambda_n^2 \frac{\varphi}{K}\right) \text{Ai}[\lambda_n^{2/3} b], \quad (26)$$

where λ_n are chosen such that $z_n = \lambda_n^{2/3} b^*$ are roots of $\text{Ai}[z_n] = 0$. The position $b = b^* < 0$ now replaces infinity $b \rightarrow -\infty$ in equation (21). The discrete equation is often more useful than the continuous form (25).

3.2 Green functions approach

In this section we derive *approximate* Green functions. The motivation is that the Green functions approach offers a convenient way to study the properties of a system. For the system under consideration, it is possible to find an approximate analytic solution in a closed form, which matches closely the exact Green function of equation (16).

The Green function $G(b, \varphi; b_0)$ is a solution of the diffusion equation (16), for the special case when the boundary condition (18) – the source of the perturbation – is the Dirac delta function

$$g(b) = \delta(b - b_0). \quad (27)$$

Then, the solution of equation (16) for a certain boundary condition $g(b)$ can be written as

$$\sigma(b, \varphi) = \int_{-\infty}^0 db_0 g(b_0) G(b, \varphi; b_0), \quad (28)$$

which is a sum over the δ -responses weighted with the function $g(b)$ in the considered radial range.

In order to find a certain Green function $G(b, \varphi; b_0)$, we again have to calculate the corresponding coefficients A_λ in equation (25), which are unfortunately still coupled. To find a way out of this problem, we derive an *approximation* to $G(b, \varphi; b_0)$, but where additional assumptions have been used. Then, this leads to a closed analytic form. In order to check the validity of these newly introduced assumptions, we also consider alternative methods.

3.2.1 Linear combination of two limiting cases

First, we consider the linearized diffusion equation (16) just in the upper left-hand part (Fig. 5b) of the disc plane ($b < 0, \varphi > 0$). The two boundary conditions (19) and (21) are now replaced by a single *artificial* one at the line $b = 0$ in the two limiting cases:

- (i) $\sigma(b, \varphi)|_{b=0} = 0$, or
- (ii) $\partial_b \sigma(b, \varphi)|_{b=0} = 0$.

Conditions (i) and (ii) determine separately two different solutions and we argue that these solutions are limiting ones for our perturbed disc problem. Condition (i) describes a situation where particles perturbed by the embedded body cannot cross the line $b = 0$ (the radial position of the perturbers). The system is driven by two opposite dynamical processes, the gravitational action that perturbs the material, and the viscous diffusion that relaxes these perturbations. While the pulse is carried with the shear, its radial profile is radially spreading in a shape of a bell owing to diffusion. The tails of this bell are growing and the whole shape has to move to the left in order

to satisfy condition (i). Thus, effectively any perturbation at $b < 0$ is pushed away from the radial position of the perturber. The interpretation of the second condition is not as straightforward – particles tend to go toward the radial location of the perturbers while they are carried by the stream. This is based on the following. The perturbation is a Dirac pulse and the radial derivative is fixed to zero on the right-hand side of the pulse all along the angle coordinate. The maximum of the radial profile of the perturbation has to be at $b = 0$, which is equivalent to condition (ii). Thus the material, while carried by the Keplerian stream, is moving to the right in order to satisfy condition (ii) along the angle φ (see also Figs 6a and b). The real situation is somewhere in between these two extreme cases and thus can be composed by a weighted sum of either part solutions (see below).

The one-mode solution is again given by equation (22), but the new boundary condition requires a certain relation between the coefficients A_λ and B_λ : (i) $A_\lambda/B_\lambda = -\sqrt{3}$ or (ii) $A_\lambda/B_\lambda = \sqrt{3}$. The general solution for the new boundary conditions, expressed in terms of the ordinary Bessel functions, is then given by

$$\sigma_\pm(b, \varphi) = \int_0^\infty A_\pm(\lambda) \times \exp\left(-\lambda^2 \frac{\varphi}{K}\right) \sqrt{-b} J_{\pm 1/3} \left[\frac{2}{3} \lambda (-b)^{3/2} \right] d\lambda, \quad (29)$$

where the + and – signs correspond to cases (i) and (ii), respectively (a convention used in the rest of this section). The ordinary Bessel functions $J_n[z]$ form a complete orthogonal set of functions over the

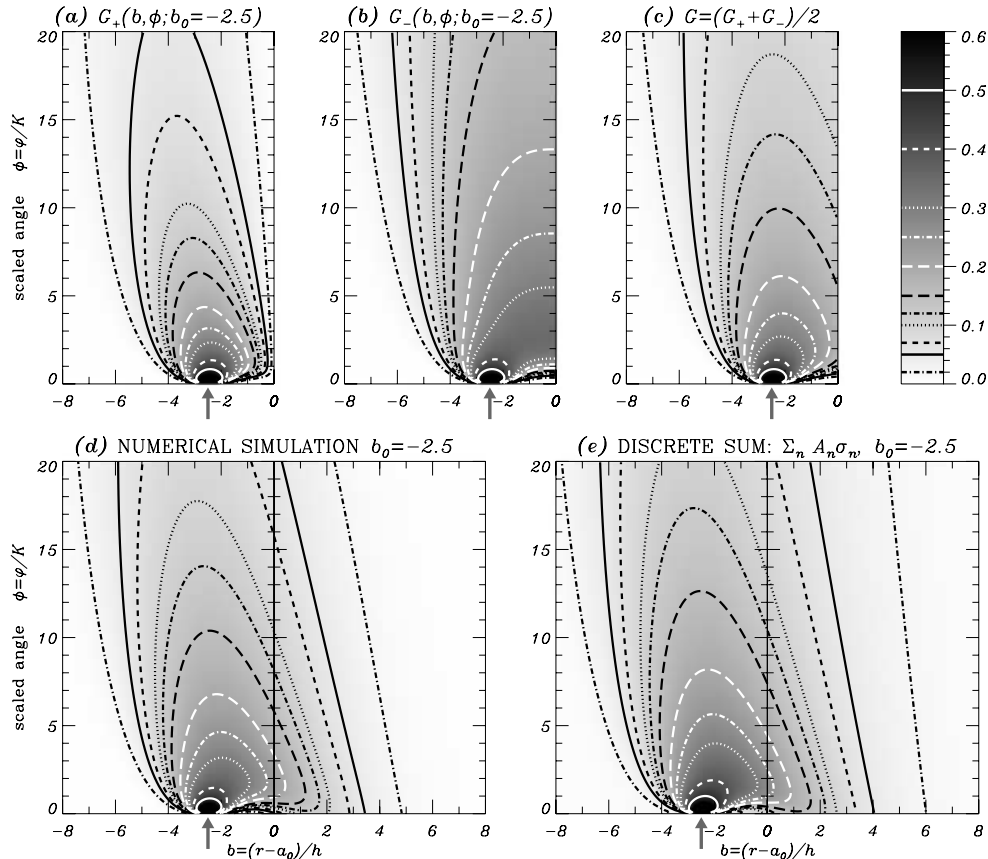


Figure 6. The Green function approximated using simplifying assumptions. Results are presented as in the grey-scale with overplotted isolines. (a) $G_+(b, \varphi)$ from equation (34). (b) $G_-(b, \varphi)$ from equation (34). (c) $G(b, \varphi)$ from equation (36) – approximate solution in a closed analytical form. (d) Result of the numerical simulation from Section 2.4 adopted for the Dirac delta function as a boundary condition. (e) Discrete sum (26) with the coefficients A_n from equation (38). The functions G_+ , G_- , and G are only applicable for $b < 0$. The position of the Dirac pulse $b_0 = -2.5, \varphi = 0$ is marked by the arrows.

interval $z \in [0, \infty)$ with a weight z in the scalar product. Different modes can then be analysed with the Fourier–Bessel theorem. Here, we quote the theorem in its most general form (Watson 1958)

$$\begin{aligned} & \int_0^\infty dk k \int_0^\infty dx x F(x) \mathcal{L}_n(kx) \mathcal{L}_n(ky) \\ &= \frac{F(y+0) + F(y-0)}{2} + \frac{2 \sin \mu \sin(n\pi - \mu)}{\pi \sin(n\pi)} \\ & \quad \times \int_0^\infty dx F(x) \frac{x^{2n} - y^{2n}}{x^2 - y^2} x^{1-n} y^{-n}, \end{aligned} \quad (30)$$

where

$$\mathcal{L}_n(z) = \frac{\sin(n\pi - \mu)}{\sin(n\pi)} J_{+n}(z) + \frac{\sin \mu}{\sin(n\pi)} J_{-n}(z). \quad (31)$$

The coefficient μ allows for a combination of J_{+n} and J_{-n} functions. The general Fourier–Bessel theorem is valid for $n \in [0, \frac{1}{2}]$. Since the second term on the right-hand side of equation (30) vanishes for $J_{+1/3}[z]$ ($\mu = 0$ in equation 31) and $J_{-1/3}[z]$ ($\mu = \pi/3$), the coefficients $A_\pm(\lambda)$ can be obtained as

$$A_\pm(\lambda) = \frac{2\lambda}{3} \int_{-\infty}^0 db (-b)^{3/2} J_{\pm 1/3} \left[\frac{2\lambda}{3} (-b)^{3/2} \right] \sigma_\pm(b, 0). \quad (32)$$

In the following, we construct a special solution – the desired approximate Green function $G_\pm(b, \varphi; b_0)$. The boundary condition is the Dirac δ function $\sigma_\pm(b < 0, \varphi = 0) = \delta(b - b_0)$ and from equation (32) we obtain

$$A_\pm(\lambda) = \frac{2}{3} \lambda (-b_0)^{3/2} J_{\pm 1/3} \left[\frac{2}{3} \lambda (-b_0)^{3/2} \right]. \quad (33)$$

In order to calculate the Green function $G_\pm(b, \varphi; b_0)$ from equation (29), we use the following identity (Watson 1958)

$$\begin{aligned} & \int_0^\infty dk k \exp(-k^2 z^2) J_n(kx) J_n(ky) \\ &= \frac{1}{2z^2} \exp\left(-\frac{x^2 + y^2}{4z^2}\right) I_n\left[\frac{xy}{2z^2}\right], \end{aligned}$$

which is valid for $n > -1$ and $|\arg(z)| < \pi/4$. Inserting equation (33) into equation (29), we arrive at the final result,

$$\begin{aligned} G_\pm(b, \varphi; b_0) &= \frac{K}{3\varphi} \sqrt{b_0^3 b} \\ & \quad \times \exp\left[\frac{K}{9\varphi}(b_0^3 + b^3)\right] I_{\pm 1/3}\left[\frac{2K}{9\varphi}(b_0 b)^{3/2}\right]. \end{aligned} \quad (34)$$

The functions G_+ and G_- are plotted in Figs 6(a) and (b), respectively.

The solution of the original problem is somewhere in between cases (i) and (ii), and an approximate solution can be expressed as the linear combination

$$G(b, \varphi; b_0) = \chi G_+(b, \varphi; b_0) + (1 - \chi) G_-(b, \varphi; b_0). \quad (35)$$

The parameter χ is in the range $\chi \in [0, 1]$, and the coefficient $1 - \chi$ in front of G_- ensures that the normalization is fulfilled for the function G at the boundary $\varphi = 0$. In combination with other methods described below, we find the best agreement for $\chi = \frac{1}{2}$. Then equation (35), expressed in terms of Airy functions, finally reads as

$$\begin{aligned} G(b, \varphi; b_0) &= \frac{\sqrt{3}}{2} (-b_0) \left(\frac{K}{3\varphi}\right)^{2/3} \\ & \quad \times \exp\left[\frac{K}{9\varphi}(b_0^3 + b^3)\right] \text{Bi}\left[\left(\frac{K}{3\varphi}\right)^{2/3} b_0 b\right]. \end{aligned} \quad (36)$$

The formula is valid for $b_0, b < 0$ and is plotted in Fig. 6(c).

3.2.2 Alternative approach

Let us answer why expression (35), with $\chi = \frac{1}{2}$, matches the exact Green function of our problem fairly well. Now, we consider the original boundary conditions (18)–(21), but we neglect the non-orthogonality of one-mode solutions. If we apply the same approach described above to calculate one-mode coefficients A_λ in equation (25), using the general Fourier–Bessel theorem (30), we will end up with a complicated set of equations owing to the second term on the right-hand side of (30). In this case the one-mode solutions are Airy functions $\text{Ai}[z]$, which are not orthogonal ($\mu = \pi/6$ in equation 31).

For the calculation of the Green function $G(b, \varphi; b_0)$, we neglect this ‘non-orthogonal’ term for the moment. Repeating the procedure of Section 3.2.1 we obtain

$$A_\lambda = 2(-b_0) \lambda^{1/3} \text{Ai}[\lambda^{2/3} b_0]. \quad (37)$$

In a second iteration, we have used this value, re-evaluated the dropped ‘non-orthogonal’ term and came up with a new expression $A_\lambda^{(2)}$. The correction to the old value (37) is just a few per cent. The coefficients A_λ in the previous equation are oscillatory (Fig. 7), thus the correction is fairly small since the integrand is the product of an oscillatory and a positive rational function. For an easier numerical calculation we multiply equation (37) by

$$\Delta\lambda = \lim_{n \rightarrow \infty} (\lambda_{n+1} - \lambda_n)$$

and we find the corresponding discrete coefficients A_n as

$$A_n(\lambda_n) = 3\pi(-b_0)(-b^*)^{-3/2} \lambda_n^{1/3} \text{Ai}[\lambda_n^{2/3} b_0]. \quad (38)$$

With this expression, the Green function in the discrete form (26) gives the solution shown in Fig. 6(e). The normalized function $A_n(\lambda_n)$ is plotted in Fig. 7.

The symbols in Fig. 7 denote the numerically obtained coefficients A_n , where we have discretized the sum (26) and the boundary condition (27). The resulting matrix equation has been solved with a standard fitting method. The resulting coefficients A_n are in excellent agreement with the predicted formula (38) shown in Fig. 7. The second iteration $A_\lambda^{(2)}$ even resolves the discrepancy for small λ .

It is easy to explain why one-mode coefficients from equation (37) give such good results. In order to form the Dirac delta pulse at the

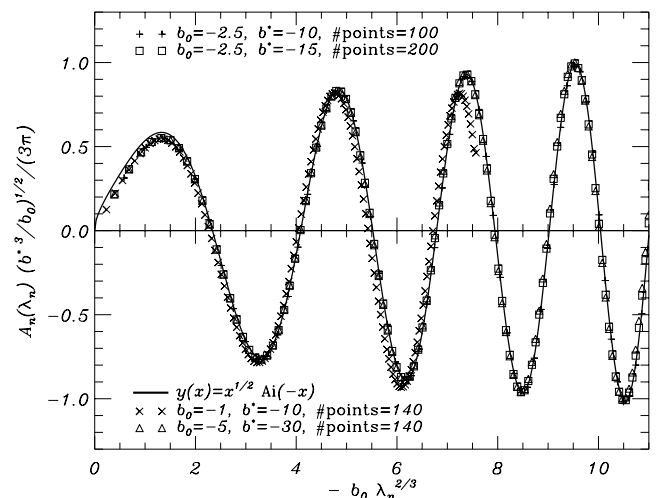


Figure 7. Comparison of discrete coefficients $A_n(\lambda_n)$. The solid line represents the predicted formula (38) and symbols represent the numerical solutions. The coefficients $A_n(\lambda_n)$ are normalized in order to allow an explicit comparison for different parameters b_0 and b^* .

boundary using oscillatory Airy Ai functions, the coefficients have to be oscillatory as well. We showed that in the simplified case with the artificial boundary conditions (see Section 3.2.1), the one-mode solution is just an ordinary Bessel function $J_{\pm 1/3}$. After summing over all modes we obtain a modified Bessel function $I_{\pm 1/3}$. We follow this reasoning, bearing in mind definitions (23) and (24). The sum of the one-mode functions Ai ($\propto J_{1/3} + J_{-1/3}$) gives approximately Bi ($\propto I_{1/3} + I_{-1/3}$), which corresponds to formula (35) for $\chi = \frac{1}{2}$. Note that for $b < 0$ the argument of Ai in equation (25) is negative, while the argument of Bi in formula (36) is positive.

As an additional test, we adopt the numerical method described in Section 2.4 to simulate directly the Green solution. We used the boundary conditions (18)–(21) and the resulting solution is shown in Fig. 6(d). We consider this solution to be the most accurate one and we use it as a reference for checking the others.

Generally, the approximate formulae, (36) and (26) with coefficients A_n in equation (38), are in a good agreement with the numerical results. The expression (36) yields an even better agreement, with generally slightly smaller values than the numerical results. The difference is less than 2 per cent. The discrete sum (26) gives a slightly worse agreement, in this case the results are a bit larger than the numerical results, but the error is less than 5 per cent. Although, the Green function (36) is an approximate solution, applicable only for $b < 0$, we use the formula in what follows, since it is written in a closed analytic form and provides a good approximation to the numerical solution of the PDE.

3.3 Non-linear diffusion equation

A power-law dependence of the kinematic viscosity on the surface density $\nu \propto \Sigma^\beta$ ($\beta > 0$) does not change the character of the solution. First, we confirmed this with our numerical simulations. The solution is again either an S-shaped structure or a gap depending on the size of the perturber and parameters of the disc. The critical size of the perturber h_{crit} is now somewhat larger compared with the case with constant kinematic viscosity ν_0 ($\beta = 0$). This is caused by an increase in the effective diffusion. The structures are also somewhat sharper compared with the case with $\beta = 0$.

In order to explain this behaviour, we consider the propagation of the surface density. The radial component of the mass flux vector $\mathbf{J} = \Sigma \mathbf{u}$, dropping the curvature and radial dependence in equation (3), is given by

$$J_r = -3(1 + \beta)\nu_0\Sigma_0 \left(\frac{\Sigma}{\Sigma_0}\right)^\beta \partial_r \left(\frac{\Sigma}{\Sigma_0}\right).$$

Regions of higher density cause a larger mass flux, and consequently, the transport is more efficient than in the lower-density regions. As a result, the gradients are steeper compared with the case with $\beta = 0$. Similar effects were discussed by Zel'dovich & Raizer (1966) in a study of non-linear thermal conduction.

However, it is known that $\beta > 0$ may lead to instabilities of the unperturbed flow (for instance, Spahn et al. 2000; Schmidt et al. 2001, and references therein). However, barring instabilities, this does not change the character of our solution. This was already pointed out by Pringle (1981). For some combinations of the coefficients β and γ in equation (5), the axisymmetric diffusion equation is solvable (e.g. $\beta = 2$ and $\gamma = \frac{9}{2}$, Lin & Pringle 1987). Furthermore, the non-linearity is taken into the account by considering the coefficient $(1 + \beta)\nu_0$ instead of ν_0 , leading in the expression (17) for the azimuthal scale K to

$$K = \frac{\Omega_0 a_0^2}{2(1 + \beta)\nu_0} h^{*3}, \quad (39)$$

where we have used the solution of the linear case (28) with the Green function (36).

4 APPLICATIONS

4.1 Characteristic scales of density patterns

In this section we discuss the azimuthal extent of the propeller solutions. Let us start with an estimate. The gravitational scale is given by the Hill radius $h^* a_0$. It measures roughly the radial scale of the stationary structure: $l_r = h^* a_0$. The viscous diffusion counteracts the gravitational scattering and the time-scale of such a process is $t_v = l_r^2/\nu_0$. During that time, the disc material will move in a corotating frame about $l_\varphi = |\Omega - \Omega_0| t_v a_0$ away from the longitude of the perturber. The angular velocity is given by $|\Omega(a_0 + l_r) - \Omega_0| = 1.5 h^* \Omega_0$ giving the azimuthal scale $l_\varphi = 1.5 a_0^2 \Omega_0 a_0 h^{*3}/\nu_0$. With this we may write

$$\frac{l_\varphi}{2\pi a_0} = \frac{3}{2\pi} K.$$

For a given disc and a perturber with a Hill scale h^* , the extensions of the induced structure are then $l_r \propto h^*$ and $l_\varphi/(2\pi a_0) \propto h^{*3}/\nu_0$.

In order to give a more accurate prediction for an azimuthal extent of the propeller structures we use the expression (28) with the Green function (36). The boundary condition $g(b)$ has to be solved simultaneously with the Markov process, but as a first approximation we can use equation (15). This equation yields the radial profile at the boundary under the assumption of uniformly distributed material that enters the scattering region. It does not differ considerably from the self-consistent profile (cf. the solid and chain lines in Fig. 3). Thus, the analytic solution with $g(b)$ approximated by equation (15) should be close to the numerical self-consistent solution.

Furthermore, we approximate the profile (15) with the two Dirac spikes as shown in Fig. 8. The first spike is located at the gap forming position $b_0 = -2.5$ with strength $I = -0.8\Sigma_0$. This strength is equal to the integral of the profile over the region where the density is less than Σ_0 as illustrated in Fig. 8. The second spike is located at $b_0 = -5$ and its the strength $I = 0.4\Sigma_0$ has been determined accordingly. It represents the disc material pushed from the gap position in the direction opposite to the radial position of the perturber. With this the density field becomes

$$\Sigma(b, \phi)/\Sigma_0 = 1 - 0.8 G(b, \phi; -2.5) + 0.4 G(b, \phi; -5). \quad (40)$$

In Fig. 9 we show the azimuthal profiles taken at the position $b = -2.5$, which corresponds to the maximum depletion along the radial direction. The numerical results are presented with symbols,

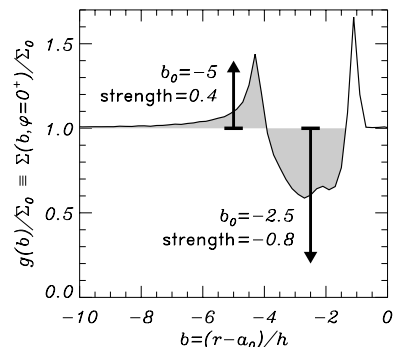


Figure 8. Sketch of the two Dirac delta functions approximating the radial profile from Fig. 3. The strength of pulses is equal to the shaded areas.

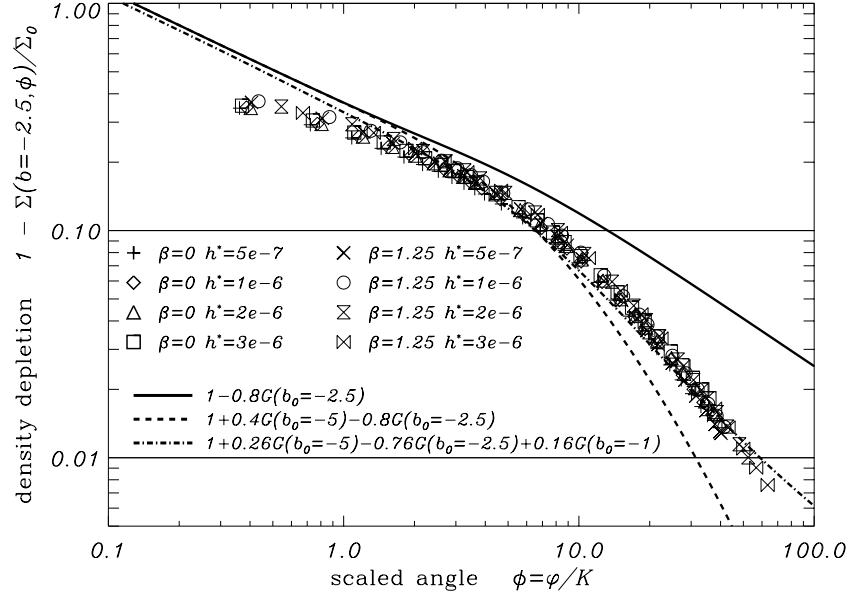


Figure 9. Azimuthal profiles of the ‘propeller’ solutions taken at $b = -2.5$, which corresponds approximately to the maximal depletion of the surface density field along the radial direction. Different symbols present the result of the numerical method, and lines correspond to combinations of Green functions.

and lines correspond to the solutions in terms of Green functions. In the figure, the angle is scaled with the corrected coefficient K from equation (39). The azimuthal profiles fall on top of each other for different sizes of the perturber h^* and density power-law coefficients $\beta \in \{0, 1.25\}$. Note, that in the numerical simulations we fully take into account curvatures and radial dependences. The single Dirac spike at $b_0 = -2.5$ gives just an order of magnitude estimate (Fig. 10a and the solid line in Fig. 9). Even better, formula (40), representing the response to two δ -spikes, captures the essential features of the propeller very well (Fig. 10b and the dashed line in Fig. 9), including the knee in the log–log plot. A better agreement cannot be expected, since the assumption of the uniformly distributed material entering the scattering region is rather crude. This is caused by the fact that the diffusion equation (4) and the Markov model of the gravitational scattering, equation (6), have to be fulfilled simultaneously. It is striking that the simple construction consisting of the two Dirac spikes is in fairly good agreement with the much more complicated numerical solution of the coupled PDE and integral equation. If we add a third spike located between the gap forming location

and the perturber, at $b_0 = -1$, and tune the spike strengths, we are able to match the propeller shape to a very good degree (Fig. 10c and the chain line in Fig. 9). The three delta-spikes mimic the complicated action of the perturber almost perfectly. For comparison, in Fig. 10(d) we show the numerical solution from Section 2.4.

The azimuthal profile in Fig. 9 falls steeply for $\phi > 10$ and as a measure for the azimuthal extension of the propeller structure we take the angle where the density perturbation is 1 per cent: $\phi_{\text{crit}} \approx 50$. Then, for the angle $\varphi = K\phi$ we obtain

$$\phi_{\text{crit}} = 2 \times 50 \frac{\Omega_0 a_0^2}{2(1 + \beta)v_0} h^{*3}. \quad (41)$$

The factor of 2 arises from the second part of the structure $\varphi < 0$, which is point symmetric to the first part $\varphi > 0$. The critical size of the perturber separating the propeller and gap is $\varphi_{\text{crit}} = 2\pi$ or

$$h_{\text{crit}}^* = \left[\frac{\pi(1 + \beta)v_0}{25 \Omega_0 a_0^2} \right]^{1/3}. \quad (42)$$

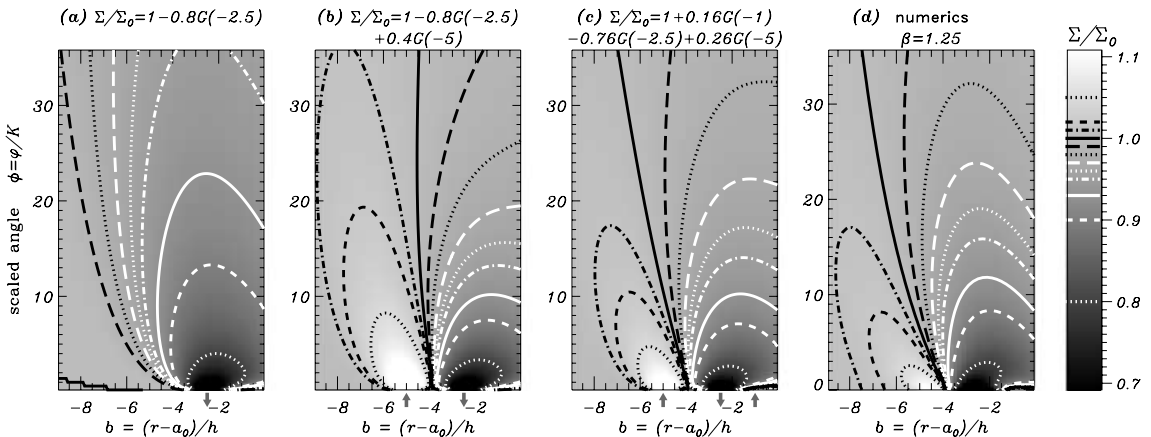


Figure 10. The surface density field corresponding to the combination of the analytic Green functions (a)–(c) and numerical simulation for the power-law-dependent kinematic viscosity $\beta = 1.25$ (d). Panels (a)–(c) correspond to solid, dashed and chain line in Fig. 9, respectively.

For small angles ϕ the analytic curves in Fig. 9 overestimate the density depletion, compared with the numerical results. This is not surprising, because small angles ϕ mean that the region is too close to the perturber and the assumption of a few Dirac delta peaks at the boundary mimicking the complex scattering is simply too crude. On the other hand, although the numerical solution is closer to reality, it also cannot resolve the vicinity of the perturber.

Further away, at larger angles ϕ , the analytic solution matches the results of the numerical simulations quite well. There, the solution is robust with respect to the details of the scattering. The reason for this robustness is the following. In the asymptotic limit $t \rightarrow +\infty$ (or $\phi \rightarrow +\infty$) each solution of the diffusion equation tends to the self-similar one. This is true, in particular, for our construction (40) and for the exact solution. They will eventually (for $\phi \rightarrow +\infty$) evolve to the self-similar solution, and their differences will become smaller and smaller. The reader can find further examples of self-similar solutions for diffusion equations and their properties in the works of Zel'dovich & Raizer (1966), Lin & Pringle (1987) and Succi & Iacono (1987).

In summary, choosing an appropriate strength for the peaks we are able to give a good approximation to the shape and the extensions of the structures. The comparison with our analytic solution shows that it is not important to match the boundary conditions *exactly*, and thus, to describe all the details of gravitational scattering. The decisive quantity for the overall structure is the strength of the perturbation. Our scattering matrix approach models the basic features of the gravitational action of a perturber in a cosmic disc. In equation (40) the strength of the perturbation enters the resulting density field linearly, and we argue that our estimate of the azimuthal size of the structure is correct at least to an order of magnitude. The critical size of the perturber h_{crit}^* (equation 42) depends on the strength through the third root, and thus, it is much less sensitive to variations.

All of these facts explain the similar estimates for the h_{crit}^* , obtained with different models in the case of dense planetary rings (Hénon 1981; Lissauer et al. 1981), and for the opening of a gap in a protoplanetary discs (Lin & Papaloizou 1986). These estimates in the case of these rather different cosmic discs will be briefly presented in the following two subsections.

4.2 Protoplanetary discs

First, we apply our results to protoplanetary cold accretion discs. Most of the protostellar disc has already been accreted by the newly formed star, and the total mass of the disc is small compared with it, i.e. self-gravity plays no role.

In the following we assume a rather simple disc model to illustrate the performance of our approach in this case. We assume a disc with a constant opening angle

$$\frac{H}{r} = \frac{c_s}{r\Omega} = 0.05, \quad (43)$$

an equation of state $p \propto \Sigma T$, and a vertically isothermal structure. These assumptions correspond to a radial temperature profile¹ $T(r) \propto r^{-1}$ (with the speed of sound $c_s^2 \propto T$). The mean thickness H follows from the vertical stratification of an isothermal disc.

The crucial parameter, besides the mass of the embedded planet, is the turbulent kinematic viscosity of the disc, parametrized in the form (Shakura & Sunyaev 1973)

$$\nu = \alpha c_s H. \quad (44)$$

The dimensionless parameter α measures the efficiency of the turbulent transport. The equation assumes that the turbulence leads to viscous transport through the action of eddies of typical size H with a turnover velocity αc_s . For our estimates we use $\alpha = 10^{-3}$, a value often used in the literature (Lubow et al. 1999; Kley 1999).

In planetary formation an interesting question is whether a gap is opened or not. Let us rewrite the threshold Hill scale (42) in terms of the mass ratio $q = M_p/M_c$ of the protoplanet M_p and the central star M_c :

$$q_{\text{crit}} = \frac{3\pi(1+\beta)v_0}{25\Omega_0 a_0^2}. \quad (45)$$

In our simplified model, the α -prescription (44) corresponds to $\beta = 0$, leading to $q_{\text{crit}} = 0.4 v_0/(\Omega_0 a_0^2)$. It is noteworthy that this expression shows the same functional form as the so-called viscosity condition for the opening of a gap found by Lin & Papaloizou (1993) (Bryden et al. 2000)

$$q_v = 40 \frac{v_0}{\Omega_0 a_0^2}, \quad (46)$$

but with a rather different pre-factor.

The criterion (45) is derived assuming that the density modulation extends from $\varphi = -\pi$ to π , and the density perturbation $\sigma = \Sigma - \Sigma_0$ of the structure at $\varphi = \pm\pi$ is 1 per cent of the unperturbed value Σ_0 . This means that even for q slightly above q_{crit} a gap has not yet fully developed (see also Section 2.4). Therefore, we define a new criterion for the formation of a gap and take a limiting density perturbation of $\sigma = 0.1 \Sigma_0$. This deviation coincides with the ‘knee’ at $\phi \approx 10$ in the azimuthal profile (Fig. 9). Beyond this distinct point, $\phi > 10$, the density perturbation decays much faster. Since the density modulation survives along the circumference, the 10 per cent depletion meets the perturber again and is scattered again and again. This leads to an even more pronounced gap, and suggests a threshold value of

$$q_{\text{gap}} = \frac{6\pi(1+\beta)v_0}{5\Omega_0 a_0^2}, \quad (47)$$

with a numerical pre-factor of ≈ 3.8 (cf. equation 46). Under our assumptions, the above three critical values of q depend only on dimensionless quantities α and H/r , but not on the radius r .

Using the numerical values introduced above ($\alpha = 10^{-3}$ and $H/r = 0.05$) we obtain $q_{\text{crit}} = 10^{-3} M_J/M_\odot = 0.31 M_\oplus/M_\odot$, $q_{\text{gap}} = 10^{-2} M_J/M_\odot = 3.1 M_\oplus/M_\odot$ and $q_v = 0.1 M_J/M_\odot = 33 M_\oplus/M_\odot$ (where M_\oplus is the mass of Earth and M_J is the mass of Jupiter). In other words, a protoplanet smaller than $q < q_{\text{crit}}$ induces a ‘propeller’. An intermediate circumference-extended structure, but not yet a full gap, is obtained for $q_{\text{crit}} < q < q_{\text{gap}}$; and a gap is opened for $q > q_{\text{gap}}$. Accordingly, the threshold q_v for opening a gap as given by Lin & Papaloizou (1986) is overestimated. Numerical simulations by Artymowicz (2000) also support this conclusion. In particular, Artymowicz showed a simulation where a protoplanet with $M_p = 25 M_\oplus$ embedded in a solar nebula with $\alpha = 0.006$ and $H/r = 0.05$ is able to open a gap. For these parameters, critical values of q are $q_{\text{gap}} = 19 M_\oplus/M_\odot$ and $q_v = 200 M_\oplus/M_\odot$, while the mass ratio of the protoplanet and star is $q = 25 M_\oplus/M_\odot$. Hence, our results are in agreement with Artymowicz’s simulations, while q_v is too large.

Our results have been obtained under the assumption of stationarity, i.e. conditions should not change considerably compared with one synodic period $t_{\text{syn}} = 4\pi/(3\Omega_0 h^*)$, which corresponds to the radial scale $l_r = h$. In other words, the planet must not grow too fast,

¹We are aware that this violates the stationarity condition for an accretion disc, but we are willing to accept this for the sake of the simplicity of the approach.

i.e. $M_p/\dot{M}_p \gg t_{\text{syn}}$, and should not migrate too quickly, $a/|\dot{a}| \gg t_{\text{syn}}$. The first condition is more restrictive. It can be estimated that under the conditions of Jupiter the criterion is fulfilled for planetary cores of approximately Earth mass and somewhat bigger. Also, curvature might play a role, so the applicability of the model is limited by $h^* \ll 1$, i.e. not too big planets. Finally, our model is two-dimensional, assuming a small thickness for the disc. It remains to be investigated whether the $H/r = 0.05$ vertical extent leads to additional effects. Numerical simulations (Lubow et al. 1999; Kley 1999; Artymowicz 2000; Kley et al. 2001) have shown that similar lateral structures (gaps and propellers) develop.

In summary, the cores of the gaseous giants, having masses $\approx 10 M_{\oplus}$, are just at the limit of where they are able to open up a gap. The formation of cores with smaller masses can occur in the regime where only azimuthally limited density modulations (the propellers) exist.

4.3 Planetary rings

We apply the model to dense planetary rings with an embedded moon acting as a perturber. Parameters typical for the B ring of Saturn are used for the numerical calculation as listed in Table 1. The particle properties of the rings are poorly constrained, and so are the effective transport coefficients of the ring flow. For definiteness we use $v_0 = 10 \text{ cm}^2 \text{ s}^{-1}$. According to local event-driven simulations of a planetary ring performed by Salo, Schmidt & Spahn (2001), the chosen kinematic viscosity would correspond to metre-sized particles. The power-law exponents in the kinematic viscosity we fix to $\gamma = 0$ and $\beta \approx 1$. The choice of $\gamma = 0$ reflects the fact that we are interested in structures of a small radial extent. A value of β close to unity is mainly caused by the finite-size effects of the collisional contributions to momentum transport (Araki & Tremaine 1986; Wisdom & Tremaine 1988).

We estimate the size of the local S-shaped structures as $L_r \approx 10h$ (see Figs 3 and 4) and

$$L_\varphi = a_0 \varphi_{\text{crit}} \approx 50 \frac{\Omega_0 h^3}{(1 + \beta)v_0}.$$

If we assume that the moonlet consists of dirty ice ($\rho = 1000 \text{ kg m}^{-3}$), we find that its radius is approximately $R \approx 0.74 h$. Using the adopted values from Table 1, for a moonlet of size $R = 50 \text{ m}$ we obtain the scales $L_r \approx 680 \text{ m}$ and $L_\varphi \approx 1300 \text{ km}$, while for a house-sized object $R = 20 \text{ m}$ we obtain $L_r \approx 270 \text{ m}$ and $L_\varphi \approx 85 \text{ km}$. The depletion of the ring density reaches a maximum of 50 per cent near the satellite. The threshold value for the circumference-extended structures reads as $R_{\text{crit}} \approx 390 \text{ m}$, while a pronounced gap would occur for $R > R_{\text{gap}} \approx 840 \text{ m}$.

There are two possible sources for errors in the application of this model to planetary rings: here we have not taken into account the influence of the gravity of the moon on the properties of the ring material. First, the satellite induces so-called wakes, beyond $|b| > 5$ (Showalter et al. 1986; Lewis & Stewart 2000). Secondly, the moon heats up the nearby material, thus the kinematic viscosity is increasing. Both phenomena are effective in the close vicinity of the moonlet only (see also Spahn & Sremčević 2000). Since the perturber is very small and the structures are very elongated (over most of the covered region of the ring), the properties of the material are close to the values of the unperturbed ring. The wakes are dissipated by inelastic collisions, and heated material is cooled down quickly. Thus, the overall properties of the model are only slightly changed.

The main outcome justifies the hope that a spacecraft such as Cassini will be able to detect ring boulders larger than 10 m in size, because the induced density structures are well within the resolution limits of its cameras.

5 SUMMARY

We have developed a model that brings together the common underlying physics of cosmic thin cold discs: planetary rings and protoplanetary discs. They differ in their spatial extensions and transport properties, but using a scaling for the geometry and the transport properties we have been able to describe them within the same model. The discs are perturbed by an embedded body (moonlet or protoplanet) and we developed an analytic approach to characterize the density features they induce gravitationally. The viscous diffusion counteracts the gravity perturbations and tends to smear out the disturbed matter. The main goal of this paper was to quantify and characterize the stationary density features that originate as a result of the interplay of the two counteractive processes.

The model consists of two parts: a probabilistic description of the gravitational scattering of an embedded body (Spahn & Wiebcke 1988) and hydrodynamical equations determining the state of the disc matter away from the perturber. The two parts of the model determine the surface density field $\Sigma(r, \varphi)$ in a self-consistent way. The gravitational action of the perturbing body is addressed with a Markov model consisting of radial states on the line that approximates the scattering region. The probabilities of the radial transitions are calculated numerically integrating the trajectories of the three-body problem for a large set of test particles. The second part of the model, the hydrodynamic description, reduces to a non-linear diffusion equation. The numerical simulation (Spahn & Sremčević 2000) showed two types of density structures: a gap and a local S-shaped density modulation (called propellers), depending on the size of the perturbing body and transport properties of the disc material.

The analytical solution of propeller states is developed using Green functions. The position and the strength of the pulse is obtained from the scattering properties of the perturbing body. The solution is approximate, but very close to the exact one, and the pulse perturbation is sufficient to explain the large-scale shape, which we confirmed by comparison with the numerical results. The reason why the pulse approximation works is that the diffusion process, or the corresponding diffusion equation, approaches the self-similar solution in the asymptotic case. In other words, the system does not remember what exactly happened at the scattering region far away (or a long time ago). What really matters is the strength of the perturbations and the transport properties of the system.

Planetary rings are especially suitable for being treated with our model: they are very thin, possible embedded moonlets are very small and the stationarity is not in question. The existence of moonlets and predictions of the model can be checked in 2004, when the spacecraft Cassini reaches the Saturnian system. Mainly using the Imaging Science Subsystem (ISS), the spacecraft will be able to resolve the important question of whether large embedded bodies (50 m up to few km) are present in the rings of Saturn? This question could not be answered by the two Voyager space-probes 20 years ago. The Cassini cameras will certainly be able to resolve these expected structures and check whether there are any moonlets or not. Information on this could also highlight the as yet unclear origin of rings, and transport properties of the ring material as well.

We showed that our model can be applied to protoplanetary discs as well. The number of detected exoplanets has steadily increased since the pioneering discovery by Mayor & Queloz (1995).

However, there are still many questions to be answered in the theory. Our model gives insights into the interaction of the protoplanetary disc and a small embedded protoplanet (with ‘small’ denoting protoplanets that do not open a complete gap in the disc). The results are important because they show that the growth of a protoplanet can be slowed down by a decoupling from the bulk of the disc. While it is computationally difficult to trace the evolution of a small protoplanet and an entire disc together, our model introduces an alternative approach to this problem. This means, long-term simulations can be performed, including accreting states (for instance, incorporated from hydrodynamical simulations). Following both the analytical solution and numerical results, we derived a new expression for the threshold protoplanet mass needed to open a gap – approximately $M_p \gtrsim 10 M_\oplus$. It is functionally the same as the standard viscous criteria (Lin & Papaloizou 1986, 1993; Bryden et al. 2000), but with a considerably smaller numerical pre-factor. This finding has been confirmed by numerical simulations performed by Artymowicz (2000), which are in favour of a smaller numerical pre-factor as well.

Further studies in this direction should first incorporate three-dimensional hydrodynamical calculations. Moreover, the scattering process should be modelled including dissipative processes such as collisions (rings) or turbulent mixing (discs). This can be achieved in combination with numerical hydrodynamical codes (Lubow et al. 1999; Artymowicz 2000; Kley et al. 2001) and, in particular, for planetary rings, with local particle simulations (Wisdom & Tremaine 1988; Salo 1991; Salo et al. 2001). The latter method directly simulates the granular nature of planetary rings in a corotating box.

Such simulations would both capture the dissipative nature of the collisions between particles in planetary rings and the turbulent viscous nature of the gas–dust fluid inside the Hill sphere.

ACKNOWLEDGMENTS

We kindly acknowledge Professor Larry W. Esposito and Dr Jürgen Schmidt for very useful discussions. This work was supported by the Deutsche Forschungsgemeinschaft, grant number Sp 384/12-1.

REFERENCES

- Abramowitz M., Stegun I.A., 1970, *Handbook of Mathematical Functions*. Dover Publications, New York
- Araki S., Tremaine S., 1986, *Icarus*, 65, 83
- Artymowicz P., 2000, in Penny A., Artymowicz P., Lagrange A.-M., Russell S., eds, *Proc. IAU Symp. 202, Planetary Systems in the Universe: Observation, Formation and Evolution*. Astron. Soc. Pac. San Francisco, in press
- Bryden G., Różyczka M., Lin D.N.C., Bodenheimer P., 2000, *ApJ*, 540, 1091
- Cuzzi J.N., Scargle J.D., 1985, *ApJ*, 292, 276
- Cuzzi J.N., Lissauer J.J., Esposito L.W., Holberg J.B., Marouf E.A., Tyler G.L., Boishchot A., 1984, in Greenberg R., Brahic A., eds, *Planetary Rings*. Univ. Arizona Press, Tucson, AZ, p. 73
- Esposito L.W. et al., 1983, *J. Geophys. Res.*, 88, 8643
- Hénon M., 1981, *Nat*, 293, 33
- Horn L.J., Cuzzi J.N., 1996, *Icarus*, 119, 285
- Ida S., Makino J., 1992, *Icarus*, 96, 107
- Kley W., 1999, *MNRAS*, 303, 696
- Kley W., D’Angelo G., Henning T., 2001, *ApJ*, 547, 457
- Lewis M.C., Stewart G.R., 2000, *AJ*, 120, 3295
- Lin D.N.C., Papaloizou J.C.B., 1986, *ApJ*, 307, 395
- Lin D.N.C., Papaloizou J.C.B., 1993, in Levy E.H., Lunine J.I., eds, *Protostars and Planets III*. Univ. Arizona Press, Tucson, AZ, p. 749
- Lin D.N.C., Pringle J.E., 1987, *MNRAS*, 225, 607
- Lissauer J.J., 1993, *ARA&A*, 31, 129
- Lissauer J.J., Shu F.H., Cuzzi J.N., 1981, *Nat*, 292, 707
- Lubow S.H., Seibert M., Artymowicz P., 1999, *ApJ*, 526, 1001
- Lüst R., 1952, *Z. Naturf.*, 7a, 87
- Lynden-Bell D., Pringle J.E., 1974, *MNRAS*, 168, 603
- Mayor M., Queloz D., 1995, *Nat*, 378, 355
- Nicholson P.D., French R.G., Tollestrup E., Cuzzi J.N., Harrington J., Matthews K., Perkovic O., Stover R.J., 2000, *Icarus*, 145, 474
- Ohtsuki K., Emori H., 2000, *AJ*, 119, 403
- Petit J.-M., Hénon M., 1986, *Icarus*, 66, 536
- Petit J.-M., Hénon M., 1987, *A&A*, 173, 389
- Poulet F., Sicardy B., Dumas C., Jorda L., Tiphène D., 2000, *Icarus*, 145, 147
- Pringle J.E., 1981, *ARA&A*, 19, 137
- Salo H., 1991, *Icarus*, 90, 254
- Salo H., Schmidt J., Spahn F., 2001, *Icarus*, 153, 295
- Schmit U., Tscharnuter W.M., 1999, *Icarus*, 138, 173
- Schmidt J., Salo H., Spahn F., Petzschmann O., 2001, *Icarus*, 153, 316
- Shakura N.I., Sunyaev R.A., 1973, *A&A*, 24, 337
- Showalter M.R., 1991, *Nat*, 351, 709
- Showalter M.R., Cuzzi J.N., Marouf E.A., Esposito L.W., 1986, *Icarus*, 66, 297
- Smith B.A. et al., 1981, *Sci*, 212, 163
- Smith B.A. et al., 1982, *Sci*, 215, 505
- Spahn F., Sponholz H., 1989, *Nat*, 339, 607
- Spahn F., Sremčević M., 2000, *A&A*, 358, 368
- Spahn F., Wiebicke H.-J., 1988, *Icarus*, 77, 124
- Spahn F., Schmidt J., Petzschmann O., Salo H., 2000, *Icarus*, 145, 657
- Stewart G.R., Lin D.N.C., Bodenheimer P., 1984, in Greenberg R., Brahic A., eds, *Planetary Rings*. Univ. Arizona Press, Tucson, AZ, p. 447
- Succi S., Iacono R., 1987, *Phys. Rev. A*, 36, 5020
- Watson G.N., 1958, *A Treatise on the Theory of Bessel Functions*. Cambridge Univ. Press, Cambridge
- Wisdom J., Tremaine S., 1988, *AJ*, 95, 925
- Zel’dovich Y.B., Raizer Y.P., 1966, *Physics of Shock Waves and High-Temperature Hydrodynamic Phenomena*. Academic Press, New York

This paper has been typeset from a $\text{\TeX}/\text{\LaTeX}$ file prepared by the author.